Posted on 21 Nov 2022 — The copyright holder is the author/funder. All rights reserved. No reuse without permission. — https://doi.org/10.1002/essoar.10504471.1 — This a preprint and has not been peer reviewed. Data may be preliminary.

Investigation of the gradient drift instability as a cause of density irregularities in subauroral polarization streams

Chirag Rathod[1], Bhuvana Srinivasan[1], Wayne A. Scales[2], and Bharat Simha Reddy Kunduri[3]

[1]Virginia Polytechnic Institute and State University
[2]Virginia Polytechnic Institute
[3]Virginia Tech

November 21, 2022

Abstract

Density irregularities have been observed in subauroral polarization streams (SAPS). One hypothesis of the cause of this ionospheric turbulence, based on the background morphology, is the gradient drift instability (GDI). This work models the GDI using a 2D electrostatic fluid model to determine if it is a viable cause of turbulence generation in SAPS. The model solves a perturbed set of continuity, energy, and current closure equations using a pseudo-spectral method. A statistical study of different velocity profiles, based on SuperDARN radar and GPS total electron content data, is used to prescribe parameters in the numerical model. The parameter space of different SAPS profiles is explored to study the effect on GDI development. As the velocity shear is initialized closer to the unstable density gradient, the GDI becomes increasingly damped. For these cases, the density and electric potential turbulence cascades obtained from the numerical model follow power laws of about -5/3 or -2, which is in agreement with observational data. If the velocity shear significantly overlaps the unstable density gradient, the GDI becomes stabilized. Decreasing the velocity gradient scale length can cause instabilities that grow inside SAPS which have turbulence cascades with power laws of -6 for the density and -8 for the electric potential. In all parameter regimes explored, the instabilities are unable to propagate through the velocity shear. Turbulence is generated for a variety of SAPS relevant conditions; therefore, the GDI has been shown to be a viable candidate for generating ionospheric irregularities in SAPS.

Investigation of the gradient drift instability as a cause of density irregularities in subauroral polarization streams

C. Rathod[1], B. Srinivasan[1], W. Scales[2], and B. Kunduri[2]

[1]Kevin T. Crofton Department of Aerospace and Ocean Engineering, Virginia Tech
[2]Bradley Department of Electrical and Computer Engineering, Virgnia Tech

Key Points:

- A statistical analysis of SAPS is conducted to understand the latitudinal velocity profile
- The GDI can cause density irregularities in SAPS at the poleward (equatorward) density gradient with an equatorward (poleward) neutral wind
- Density irregularities cannot propagate through velocity sheared regions

Corresponding author: Bhuvana Srinivasan, `srinbhu@vt.edu`

Abstract

Density irregularities have been observed in subauroral polarization streams (SAPS). One hypothesis of the cause of this ionospheric turbulence, based on the background morphology, is the gradient drift instability (GDI). This work models the GDI using a 2D electrostatic fluid model to determine if it is a viable cause of turbulence generation in SAPS. The model solves a perturbed set of continuity, energy, and current closure equations using a pseudo-spectral method. A statistical study of different velocity profiles, based on SuperDARN radar and GPS total electron content data, is used to prescribe parameters in the numerical model. The parameter space of different SAPS profiles is explored to study the effect on GDI development. As the velocity shear is initialized closer to the unstable density gradient, the GDI becomes increasingly damped. For these cases, the density and electric potential turbulence cascades obtained from the numerical model follow power laws of about -5/3 or -2, which is in agreement with observational data. If the velocity shear significantly overlaps the unstable density gradient, the GDI becomes stabilized. Decreasing the velocity gradient scale length can cause instabilities that grow inside SAPS which have turbulence cascades with power laws of -6 for the density and -8 for the electric potential. In all parameter regimes explored, the instabilities are unable to propagate through the velocity shear. Turbulence is generated for a variety of SAPS relevant conditions; therefore, the GDI has been shown to be a viable candidate for generating ionospheric irregularities in SAPS.

Plain Language Summary

Turbulence in the ionosphere is important to understand because it can negatively impact radio communication signals such as GPS signals. For example, when GPS signals travel through a turbulent region in the ionosphere, a device's position estimates become less accurate. This work helps scientists understand how turbulence is generated in the ionosphere by simulating a phenomenon called subauroral polarization streams (SAPS). SAPS are a region in the ionosphere of large westward velocity, in which turbulence has been observed. The SAPS velocity is a function of latitude. A particular phenomenon called the gradient drift instability (a plasma instability) is hypothesized to be a possible cause of the observed turbulence. This study tests this hypothesis in order to understand the generation of turbulence under different velocity profiles observed in SAPS. Findings suggest that if turbulence occurs outside (or inside) of the velocity region, then it stays outside (or inside) of the velocity region. Turbulence generated in the simulations agrees with turbulence observed in real world data, which suggests that this hypothesis could be correct.

1 Introduction

Subauroral polarization streams (SAPS) are regions of enhanced westward plasma flow generated by an $\mathbf{E} \times \mathbf{B}$ drift, which is driven by a poleward electric field (Foster & Burke, 2002) These plasma flows are accompanied by density troughs (Spiro et al., 1978). They occur in the dusk-midnight sector and have a latitudinal width of a few degrees. In the literature, sub-auroral ion drifts (SAID) or polarization jets (PJ) are other terms that have been used to describe narrow SAPS. The convection velocities can range from hundreds to thousands of meters per second. Many statistical studies have been conducted to understand the variations of velocity profiles. The locations of the peak velocity, latitudinal widths, and occurrence probabilities have been studied under different geomagnetic conditions using the Millstone Hill Radar, DMSP satellite, and SuperDARN radar data (Foster & Vo, 2002; Wang et al., 2008; Erickson et al., 2011; Kunduri et al., 2017).

The same instruments have also observed small-scale density irregularities within the large-scale structure (Mishin et al., 2003; Foster et al., 2004; Oksavik et al., 2006;

Mishin & Blaunstein, 2008). Several hypotheses exist to explain the cause of these density irregularities. Based on the geometry of the trough density gradients and background electric field, it is possible that the gradient drift instability (GDI) is causing the density irregularities (Ossakow et al., 1978). The GDI (Simon, 1963; Hoh, 1963) is an interchange instability that occurs in an inhomogeneous plasma in background electric and magnetic fields. A difference in ion-neutral and electron-neutral collision frequencies causes a charge separation that, in certain geometries, leads to instability growth. The GDI theory is extensive and covers many regions in the ionosphere (Ossakow et al., 1978; Makarevich, 2014, 2019). Studies show that velocity shear can stabilize short wavelength modes in the GDI (Perkins & Doles III, 1975; J. Huba et al., 1983; J. D. Huba & Lee, 1983). This work examines the effect of different velocity profiles, which have been observed in SAPS, on GDI growth and corresponding turbulence generation.

A large body of literature exists on the modeling of the GDI from a fundamental physics perspective (Mitchell Jr et al., 1985; Gondarenko & Guzdar, 1999; Guzdar et al., 1998). Much of the previous work on modeling SAPS has considered global SAPS dynamics (Zheng et al., 2008; Yu et al., 2015; Lin et al., 2019). The highest resolution of these models is on the order of 1°, which is not sufficient to model smaller turbulence generating density irregularities on spacial scales of tens to hundreds of meters. The mathematical model developed by M. Keskinen et al. (2004) to study instability development in SAPS is used as a motivation for this work's novel approach to studying ionospheric turbulence in SAPS.

Measurements from SuperDARN (Super Dual Auroral Radar Network) radars provide relevant input parameters for the numerical model. SuperDARN radars detect the Doppler shift of High Frequency (HF) waves coherently backscattered off of decameter scale density irregularities. This acts as a proxy for the perpendicular ion convection velocity (Ruohoniemi et al., 1987). SuperDARN's network spans both hemispheres and provides continuous measurements of the ionosphere at a 1-2 minute cadence (Chisham et al., 2007).

This paper is organized as follows. Section 2 describes a phenomenological overview of SAPS, the mathematical model derived using reasonable ionospheric assumptions for relevant parameter regimes, and a computational model used to numerically solve for the nonlinear dynamics. models. Section 3 provides a statistical analysis to understand the parameter space of latitudinal SAPS profiles which are used to initialize the simulation. Section 4 presents a parameter study exploring the previously described parameter space to understand how the GDI develops in different regimes. Comparisons are made to observed turbulence spectra. Section 5 is a summary of the results and conclusions.

2 Model

2.1 Phenomenological Model

The poleward electric field that drives the westward SAPS convection is a result of magnetosphere-ionosphere coupling through the current closure of Region 2 field-aligned currents (Foster & Burke, 2002). This electric field then maps down into the ionosphere, flowing into the collocated lower conductivity density trough. The trough is then made steeper through increased recombination due to the larger frictional heating (Schunk et al., 1976). To induce the F region GDI, the neutral wind in the north-south direction is considered. Figure 1 shows the geometry of how this is modeled, the coordinate system, and directions of gradients and fields. The SAPS electric field is set as the background electric field in the simulation. Since only motion perpendicular to the magnetic field is considered in this model, the simulation domain is in the xy plane.

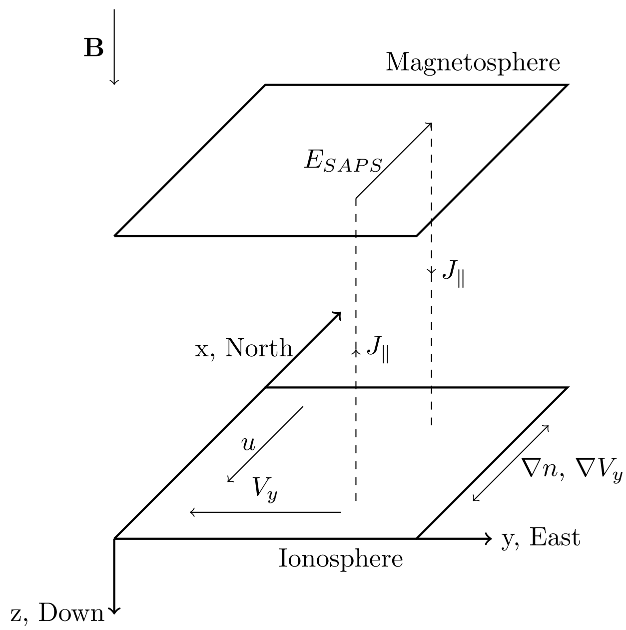

Figure 1. A diagram of the model geometry and coordinate system where x is North, y is East, and z is down. The magnetic field is purely in z. Only motion perpendicular to the magnetic field is considered. Thus, the simulation domain is in the xy plane. The background SAPS velocity is in $-y$. The density and velocity gradients are in x. The neutral wind that drives the GDI is in $-x$. The initialized electric field that drives the westward SAPS flow, E_{SAPS}, is in x. Though, this model is only 2 dimensional, the parallel current is shown in this diagram to provide a physical understanding of the electric field mapping from the magnetosphere down to the ionosphere.

2.2 Mathematical Model

A 2D fluid model is developed to study ionospheric turbulence perpendicular to the magnetic field. The model is an adaptation of M. Keskinen et al. (2004) with the inclusion of inertial effects. The inertial effects are important in understanding the plasma dynamics of the less collisional F region as well as studying the effect of velocity shear on the GDI. Additionally, the frictional heating terms are neglected in an effort to simplify the governing equations. The continuity, momentum, and energy equations are

$$\frac{\partial n_\alpha}{\partial t} + \nabla \cdot (n_\alpha \mathbf{V}_\alpha) = D\nabla^2 n_\alpha \tag{1}$$

$$n_\alpha\Big(\frac{\partial}{\partial t} + \mathbf{V}_\alpha \cdot \nabla\Big)\mathbf{V}_\alpha = \frac{q_\alpha n_\alpha}{m_\alpha}(\mathbf{E} + \mathbf{V}_\alpha \times \mathbf{B}) - \frac{\nabla P_\alpha}{m_\alpha} - n_\alpha \nu_{\alpha n}(\mathbf{V}_\alpha - \mathbf{u}) \tag{2}$$

$$\frac{3}{2}n_\alpha k_B \frac{\partial T_\alpha}{\partial t} + \frac{3}{2}n_\alpha k_B \mathbf{V}_\alpha \cdot \nabla T_\alpha + n_\alpha k_B T_\alpha \nabla \cdot \mathbf{V}_\alpha = 0, \tag{3}$$

where α denotes the species (i for ions and e for electrons), n is the number density, $\mathbf{V}$ is the velocity, q is the electric charge, m is the mass, $\mathbf{E}$ is the electric field, $\mathbf{B}$ is the magnetic field, P is the pressure, $\nu_{\alpha n}$ is the collision frequency with neutral particles, T is the temperature, and D is an artificial diffusion constant. The ideal gas law, $P_\alpha = n_\alpha k_B T_\alpha$, is used as the equation of state where k_B is the Boltzmann constant. The collision frequencies are self-consistently calculated using $\nu_{\alpha n} = n_n V_{Th_\alpha} \sigma_{\alpha n}$, where n_n is the neutral particle number density, V_{Th} is the thermal velocity, and σ is the collision cross-section. The temperature equations are included in this model but are observed to have negligible impact and thus are not considered in the remainder of this paper. Eq. 2 is used to derive the ion and electron velocities in terms of zeroth and first order in $1/\Omega_\alpha$, where Ω is a gyrofrequency. The resulting velocities are

$$\mathbf{V}_e^0 = \frac{\mathbf{E}\times\mathbf{B}}{B^2} + \frac{\nabla P_e \times \mathbf{B}}{eB^2 n_e} \tag{4}$$

$$\mathbf{V}_e^1 = -\frac{\nu_{en}}{\Omega_{ce}}\frac{\nabla P_e}{en_e B} - \frac{\nu_{en}}{B\Omega_{ce}}\Big(\mathbf{E} + \mathbf{u}\times\mathbf{B}\Big) - \frac{1}{B\Omega_{ce}}\Big(\frac{\partial}{\partial t} + \mathbf{V}_{\mathbf{E}\times\mathbf{B}}\cdot\nabla\Big)\mathbf{E} \tag{5}$$

$$\mathbf{V}_i^0 = \frac{\mathbf{E}\times\mathbf{B}}{B^2} - \frac{\nabla P_i \times \mathbf{B}}{eB^2 n_i} \tag{6}$$

$$\mathbf{V}_i^1 = -\frac{\nu_{in}}{\Omega_{ci}}\frac{\nabla P_i}{en_i B} + \frac{\nu_{in}}{B\Omega_{ci}}\Big(\mathbf{E} + \mathbf{u}\times\mathbf{B}\Big) + \frac{1}{B\Omega_{ci}}\Big(\frac{\partial}{\partial t} + \mathbf{V}_{\mathbf{E}\times\mathbf{B}}\cdot\nabla\Big)\mathbf{E}. \tag{7}$$

Only the zeroth order velocities, Eqs. 4 and 6, are used in the continuity and energy equations, Eqs. 1 and 3. The plasma is assumed to be quasineutral ($n_i = n_e = n$) so only one continuity equation is used. It can be shown that the diamagnetic drift does not affect the continuity equation so only the $\mathbf{E}\times\mathbf{B}$ drift is used as its velocity. The plasma is in an electrostatic regime such that $\mathbf{E} = -\nabla\phi$, where ϕ is the electric potential. The system is closed using the current closure equation, $\nabla\cdot\mathbf{J} = 0$, where $\mathbf{J} = ne(\mathbf{V}_i - \mathbf{V}_e)$ is the current density. The zeroth and first order velocities are used to calculate $\mathbf{J}$. Thus, the resulting continuity and current closure equations are

$$\frac{\partial n}{\partial t} - \frac{\nabla\phi\times\mathbf{B}}{B^2}\cdot\nabla n = D\nabla^2 n \tag{8}$$

$$\nabla\cdot\Big(n\nabla\frac{\partial\phi}{\partial t}\Big) = \Big(\frac{1}{\Omega_{ci}}+\frac{1}{\Omega_{ce}}\Big)^{-1}\Big[-\frac{\nu_{in}}{e\Omega_{ci}}\nabla^2 P_i + \frac{\nu_{en}}{e\Omega_{ce}}\nabla^2 P_e + \Big(\frac{\nu_{in}}{\Omega_{ci}}+\frac{\nu_{en}}{\Omega_{ce}}\Big)\Big(\mathbf{u}\times\mathbf{B}\cdot\nabla n - \nabla\cdot[n\nabla\phi]\Big)\Big] - \nabla\cdot\Big(n\mathbf{V}_{\mathbf{E}\times\mathbf{B}}\cdot\nabla\nabla\phi\Big). \tag{9}$$

The current closure equation implies that the system is in the frame of reference of the neutral particles such that constant applied electric field is defined by the neutral wind, $\mathbf{E}_0 = \mathbf{u}\times\mathbf{B}$, which is what drives the GDI in this model.

The turbulence development in SAPS is observed to occur on faster time scales than the overall background densities and velocities in SAPS. Therefore, a perturbed model is developed to allow for an unchanging background. The forcing of maintaining a constant background effectively acts as a method of accounting for the other physics that helps maintain a quasi-equilibrium of SAPS but are not included in this model, such as production, losses, and parallel transport. The primitive variables, ϕ, n, T_i, and T_e, are separated into background and perturbed quantities, e.g. $n = n_{bg} + n_p$. Terms containing only background quantities are removed and only terms containing perturbed quantities are retained. Based on the geometry of this problem, the continuity and temperature residual terms already satisfy this criterion. Thus, this method only needs to be applied to the continuity source term and the current closure equation resulting in

$$\frac{\partial n}{\partial t} - \frac{\nabla\phi\times\mathbf{B}}{B^2}\cdot\nabla n = D\nabla^2 n_p \tag{10}$$

$$\begin{aligned}\nabla\cdot\Big(n\nabla\frac{\partial\phi_p}{\partial t}\Big) = \Big(\frac{1}{\Omega_{ci}}+\frac{1}{\Omega_{ce}}\Big)^{-1}\Big[&-\frac{\nu_{in}}{e\Omega_{ci}}\nabla^2 P_{i_p} + \frac{\nu_{en}}{e\Omega_{ce}}\nabla^2 P_{e_p} + \\ &\Big(\frac{\nu_{in}}{\Omega_{ci}}+\frac{\nu_{en}}{\Omega_{ce}}\Big)\Big(\mathbf{u}\times\mathbf{B}\cdot\nabla n_p - \nabla\cdot[n_p\nabla\phi + n_{bg}\nabla\phi_p]\Big)\Big] \\ &- \nabla\cdot\Big(n_{bg}\mathbf{V}_{\mathbf{E}\times\mathbf{B}_{bg}}\cdot\nabla\nabla\phi_p + n_{bg}\mathbf{V}_{\mathbf{E}\times\mathbf{B}_p}\cdot\nabla\nabla\phi + n_p\mathbf{V}_{\mathbf{E}\times\mathbf{B}}\cdot\nabla\nabla\phi\Big).\end{aligned} \tag{11}$$

2.3 Computational Methods

The equations are spatially discretized with a pseudo-spectral method using a Fourier basis (Canuto et al., 2012). Thus, the spatial derivatives are converted into algebraic expressions resulting in a set of ordinary differential equations (ODEs) in time. The discretization method used requires the boundary conditions to be periodic in all dimensions. The current closure equation has a nonlinear time derivative term, $\nabla\cdot(n\nabla\partial\phi_p/\partial t)$, that cannot be easily isolated. Therefore, an iterative method is used to first calculate $\partial\phi_p/\partial t$. Thus, the system of equations is now a set of linear temporal ODEs. The system is evolved in time using a four-stage fourth order Runge-Kutta method.

3 Data-relevant Problem Setup

The problem setup for the numerical model is based on measurements from the mid-latitude SuperDARN radars and GPS TEC. In this study, data from the U.S. mid-latitude radars are used to analyze SAPS flows (Kunduri et al., 2017). The SAPS are assumed to be L-shell aligned in the region of interest, and the line-of-sight velocities are corrected by a cosine factor to yield the westward flow component. The median and standard deviation in these westward velocities are then calculated to create latitudinal profiles at different MLTs in the dusk-midnight sector. Global Positioning System (GPS) Total Electron Content (TEC) measurements provided by the Madrigal database are used to analyze the location and depth of the mid-latitude trough. The TEC measurements of the ionosphere describe the total number of electrons in a cylinder of cross-sectional area of 1 m^2 that extends vertically above a given point on the Earth all the way through the ionosphere; 1 TEC unit (TECU) is 10^{16} electrons/m^2. The TEC data are processed using the minimum scallop estimation approach (Rideout & Coster, 2006) and are binned into $1^\circ\times1^\circ$ cells with an update every 5 minutes. The median filtering technique (Thomas et al., 2013) is used to process the global GPS TEC maps to improve the spatial coverage provided by the distributed receivers. Finally, similar to the velocities derived from SuperDARN, the median and standard deviation in TEC values are calculated to create latitudinal profiles at different MLTs.

Figure 2 shows the TEC and velocity profiles at 20 MLT of a SAPS event that occurred on May 2, 2013, with annotations representing important velocity profile parameters that are analyzed in this work. The distance between the location of the center of the poleward density gradient and the location of the maximum velocity is defined as d, with positive defined such that the maximum velocity is equatorward of the poleward density gradient. There is uncertainty in the velocity measurement, and the velocity can exist anywhere between the error bars. Since velocity shear has a stabilizing effect on the growth of the GDI, it is possible that there are regions in SAPS that could have large widths of constant velocity. The thick black line in Figure 2(b) shows one such possibility of this region, whose width is defined as w. In this example, when accounting for the uncertainty, the velocity could be a constant 822 m/s for the entire region from 59.5° to 61.5° MLAT. All of the regions of constant velocity considered in this study include the maximum velocity.

Figure 2 represents a singular latitude profile at a singular MLT of a singular SAPS event. SAPS profiles vary largely in shape and location with respect to the density trough (Foster & Vo, 2002; Wang et al., 2008; Erickson et al., 2011; Kunduri et al., 2017). The parameters of importance that can change between profiles are d, w, minimum velocity gradient scale length, and maximum possible constant velocity in the region of w. An analysis of 10 different SAPS events is conducted to understand the parameter space of density and velocity profiles. For each event, latitudinal profiles at different MLTs are analyzed for a total of 86 velocity profiles and 100 TEC profiles. Of the different velocity and TEC profiles, 42 of them overlap in time and location. The goal of this analysis is to determine the initial profiles and parameters that can be used to study the irregularity development in SAPS. Due to the uncertainty in the measurements, the individual

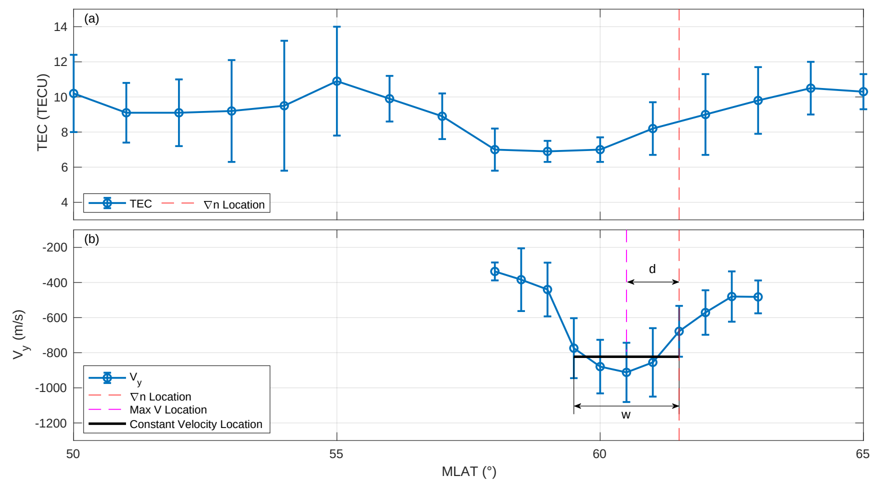

Figure 2. Latitudinal TEC (a) and velocity (b) profiles at 20 MLT of a SAPS event that occurred on May 2, 2013. The red dashed lines indicate the location of the center of the poleward density gradient. The magenta dashed line indicates the location of the maximum velocity. The distance, d, represents the distance between the location of the poleward density gradient and the location of maximum velocity, accounting for the uncertainty. The thick black line represents a region in which, accounting for the uncertainty, there can be a region of constant velocity (maximum of 822 m/s). The width of this region is defined as w.

profiles can vary between the error bounds. This can give different possible parameters for the velocity profiles. Therefore, all of the calculations done on these data choose values that optimize the particular parameter for GDI growth. For example, the maximum velocity is calculated by taking the maximum of the sum of the mean value and the uncertainty.

The velocity gradient scale length is calculated using $L_V^g = V(\partial V/\partial x)^{-1}$. The velocity derivative is calculated using a central difference method. Figure 3(a) shows the histogram of minimum L_V^g, which varies from 10 to 200 km. The histogram for the distance from the location of the maximum velocity to the location of the center of the poleward density gradient, d, varies from -230 to 580 km, as shown in Figure 3(b). The maximum velocity location is limited to be below 66° to prevent capturing effects from the auroral oval. Due to the uncertainty, it is possible that there can be large latitudinal regions of constant velocity. Figure 3(c) shows a histogram of the largest distance of possible constant velocity, w, that includes the maximum velocity point. It is shown that w can vary from 100 to 1000 km. A histogram of the maximum possible constant velocity in this region is shown in Figure 3(d) and varies from 200 to 1400 m/s.

The initial conditions are functions of only x since they represent the latitudinal profiles of SAPS densities and velocities at approximately 300 km in altitude. Examples of the initial conditions used are shown in Figure 4. The plasma density at a specific altitude is approximated to have the same shape as the TEC data, which can be approximated as two hyperbolic tangent functions,

$$n_{bg} = n_0\left(a_1 \tanh\left[\frac{x - x_{N_E}}{L_{N_E}}\right] + a_2 \tanh\left[\frac{x - x_{N_P}}{L_{N_P}}\right] + c\right), \tag{12}$$

where n_0 is a reference density, L_N is a length scaling factor, x_N is the location of the density gradient, subscripts E and P denote the equatorward and poleward sides respectively, and a_1, a_2, and c are constants chosen to have a reasonably good fit to the data. The density initial condition does not change for any simulation in Section 4.

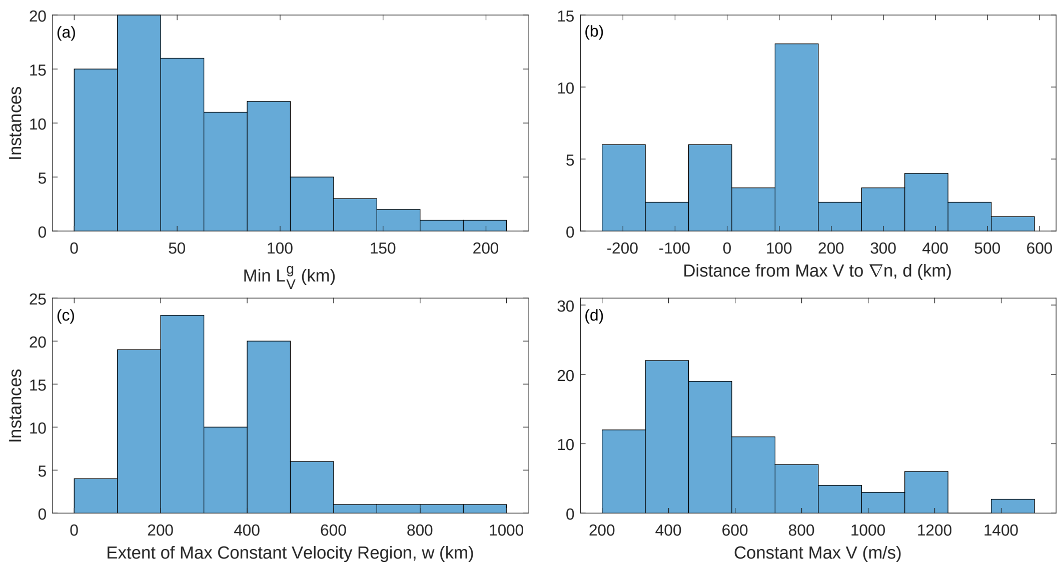

Figure 3. Histograms of different latitudinal TEC and velocity profile parameters for 10 different SAPS events across multiple MLT cuts. Panel (a) shows the minimum velocity gradient scale length, L_V^g, which varies from 10 to 200 km. Panel (b) shows the distance between the location of the maximum velocity and the location of the center of the poleward density gradient, d, which varies from -230 to 580 km, where positive is defined as the peak velocity being equatorward of the poleward density gradient. It is possible that some of the mean profiles have large regions of constant velocity due to the uncertainties of data collection. Panel (c) shows the largest region of possible constant velocity around the peak velocity location, whose width is defined as w, which varies from 100 to 1000 km. Panel (d) shows the largest possible constant velocity, which varies from 200 to 1400 m/s, in the region of w.

Based on Figure 2, the velocity is well approximated by a hyperbolic secant-squared function,

$$V_{y_{bg}}^s = V_0^s \operatorname{sech}^2\left[\frac{x - x_{N_P} + d}{L_V^s}\right], \tag{13}$$

where V_0^s is a reference velocity, L_V^s is a length scaling factor, and d is the distance between the function extremum and the poleward density gradient location as defined in Figure 2. The effect of changing d in the velocity initial condition is considered in Section 4.

Changing the velocity gradient scale length in a parameter study allows for a better understanding of the physics of the irregularity growth. However, changing L_V^s in Eq. 13 not only changes the steepness of the gradient but also the total velocity profile width. A set of two hyperbolic tangent functions,

$$V_{y_{bg}}^t = \frac{V_0^t}{2}\left(\tanh\left[\frac{x - x_{N_P} + w}{L_V^t}\right] - \tanh\left[\frac{x - x_{N_P}}{L_V^t}\right]\right), \tag{14}$$

where V_0^t is a reference velocity and w is the distance between the equatorward and poleward velocity gradients (as defined in Figure 2), allow for the gradient scale length and the width of the profile to be changed independently. The effects of changing w are considered in Section 4.

All simulations are initialized with a random noise density perturbation of $\pm 10^{-6} n_0$. Table 1 lists variables corresponding to approximately 300 km in altitude (the approximate altitude of the SuperDARN measurements from Figure 2) that are used in this study

Table 1. Nominal Simulation Parameters

Variable	Value
n_0	10^{11} m^{-3}
x_{N_E}	220 km
x_{N_P}	525 km
L_{N_E}	50 km
L_{N_P}	75 km
a_1	-0.30
a_2	0.75
c	2.05
$T_i = T_e = T$	1000 K
Ion Species	O^+
Neutral Species	O
n_n	10^{14} m^{-3}
D	10^2 to 8×10^4 m^2/s
$[k_{x_{max}} k_{y_{max}}]$	[2.14, 0.804] km^{-1}
u_x	-500 to -100 m/s
u_y	0 m/s
B	5×10^{-5} T
V_0^s	-500 m/s
V_0^t	-1000 m/s
L_V^s	34 km
L_V^t	10 km
d	75 to 175 km
w	125 -to 305 km

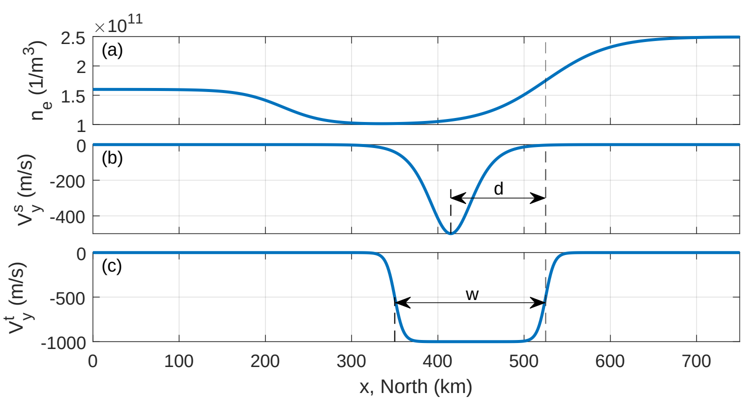

Figure 4. Plots of the initial conditions based on values from Table 1. The functions vary in x from 0 to 750 km. Panel (a) shows the plasma density based on Eq. 12. This initial condition is used for the entirety of the study. Panel (b) shows the y direction velocity based on Eq. 13 where $V_0^s = -500$ m/s, $L_V^s = 34$ km, and $d = 110$ km. This initial condition is used to study the effect of changing d on instability development. Panel (c) shows the y direction velocity based on Eq. 14 where $V_0^t = -1000$ m/s, $L_V^t = 10$ km, and $w = 175$ km. This initial condition is used to study the effects of changing L_V and w on instability development.

as well as ranges of values used. The neutral wind for all of these simulations is chosen to be equatorward since this occurs frequently in storm-time conditions (Buonsanto, 1999). The substantial westward neutral winds that develop in SAPS (Zhang et al., 2015) are not considered in this model, as they do not greatly impact the growth of the F region GDI.

4 Parameter Study

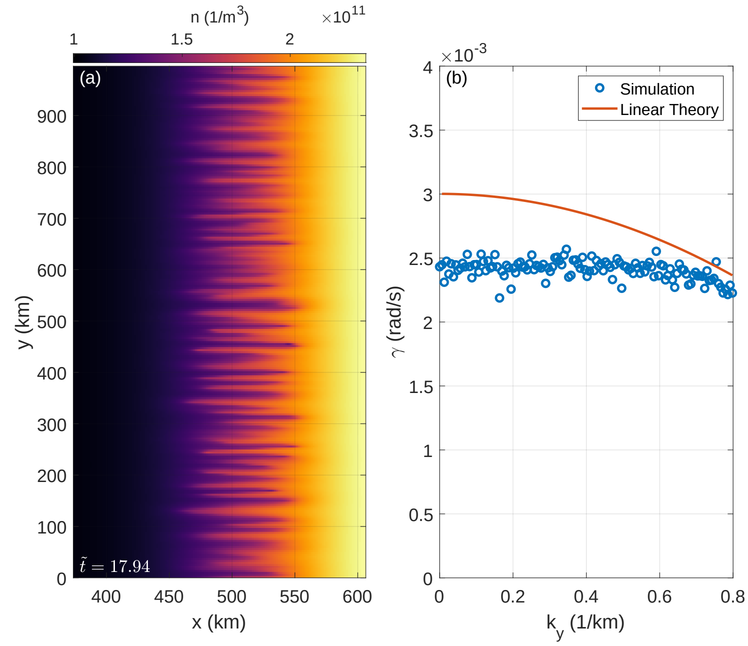

Figure 5. Results of a shearless GDI simulation. Panel (a) shows the density evolution which matches GDI behavior qualitatively. Thin fingers are seen growing into thicker tips which are secondary Kelvin-Helmholtz instabilities. Panel (b) shows the comparison of the instability growth rate between simulation (blue circles) and theory (red line) with good agreement (at most a 26.5% difference). The differences can likely be explained by nonlocal effects or the addition of inertia in this model.

The numerical model is first validated by performing a classical GDI simulation in the absence of any velocity shear prior to understanding the impact of velocity shear on irregularity development. Figure 5(a) presents the evolution of the GDI qualitatively, showing several features of classic GDI growth such as long thin fingers that grow to eventually have thicker tips, which are an indication of the onset of secondary Kelvin-Helmholtz instabilities. This agrees with previous work on the collisional GDI, e.g. Mitchell Jr et al. (1985) and Gondarenko and Guzdar (1999). Based on the geometry of the density gradient and the background southward neutral wind, the GDI is expected to grow (stabilize) at the poleward (equatorward) density gradient. Therefore, only the regions around the poleward density gradient are shown in this paper. Figure 5(b) shows the comparison of the simulation growth rate to the local linear theory growth rate. The full functional form is calculated based on Eq. 16 in Makarevich (2014), but the results show that the simulation plasma is in the F region limit. The simplified F region growth rate formula, accounting for the numerical diffusion, is

$$\gamma_{GDI} = -\frac{u_x}{L_N^g} - Dk^2, \tag{15}$$

where L_N^g is the density gradient scale length (Ossakow et al., 1978). The simulation growth rate has at most a 26.5% difference from the analytical growth rate, which can possibly be explained by nonlocal effects and the inclusion of inertia in this model (Ossakow et al., 1978; Mitchell Jr et al., 1985). Since the visual growth of the instability is highly dependent on the initial perturbation amplitude and artificial numerical diffusion, the simulation times are presented non-dimensionally as maximum GDI growth periods, $\tilde{t} = |u_x t / L_N^g|$. For these same reasons, the relative differences in times between simulations should be considered as opposed to the absolute times to understand the effects of different velocity profiles on instability evolution.

A broad parameter study is conducted based on the parameter space explored in Figure 3. The effect of varying the velocity gradient scale length, the latitudinal width, and the location of the velocity profile with respect to the poleward density gradient on density irregularity generation is investigated.

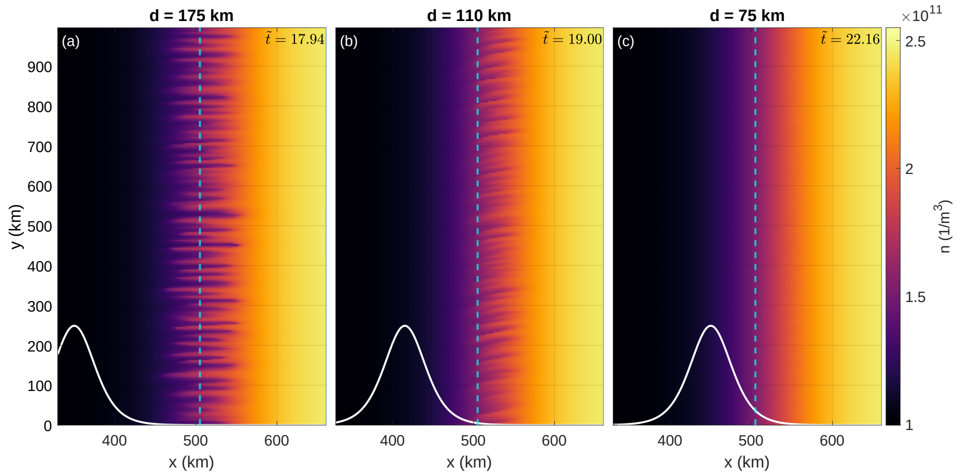

Figure 6. Plots of plasma density using Eq. 13 for the V_y initial conditions with $V_0^s = -500$ m/s, $L_V^s = 34$ km, and d varying from 75 to 175 km. The solid white curve represents the location of the velocity profile. The dashed cyan line is the location of maximum GDI growth based on Eq. 15. When the velocity is far from the density gradient, as in Panel (a), the GDI grows unimpeded at the location of maximum GDI growth. When the velocity shear is initialized closer to the density gradient, as in Panels (b) and (c), the GDI is damped and relatively small growth occurs poleward of the maximum GDI growth location.

Figure 6 shows how the GDI develops when the velocity profile is in different locations using Eq. 13 for V_y with $V_0^s = -500$ m/s and $L_V^s = 34$ km. Since the location of SAPS can vary, the quantity d is varied from 75 to 175 km. The white curve represents the velocity profile and the dashed cyan line represents the maximum GDI growth location based on Eq. 15 (equivalently the location of minimum density gradient scale length). When the velocity profile is located far away from the density gradient, as in Figure 6(a), a traditional GDI develops that looks almost identical to the development in Figure 5, with the growth occurring at the maximum GDI growth location. The implication here is that if the velocity is sufficiently far away from the density gradient, then the GDI initially evolves as though there is no velocity present. When the velocity profile is closer to the density gradient, as in Figure 6(b), GDI growth still occurs but at a slower rate, taking approximately two additional growth periods to reach a similar growth amplitude. The velocity shear appears to have a stabilizing effect on GDI growth, which is consistent with nonlocal linear theory (Perkins & Doles III, 1975; J. Huba et al., 1983; J. D. Huba & Lee, 1983). Because of this effect, the location of the instability growth has shifted poleward of the maximum GDI growth location to a new location of fastest growth. When the velocity profile is even closer to the density gradient, as in Figure 6(c), the GDI appears to be completely damped with no visual growth. This suggests that for the GDI to cause density irregularities, the velocity shear needs to be sufficiently equatorward of the poleward density gradient.

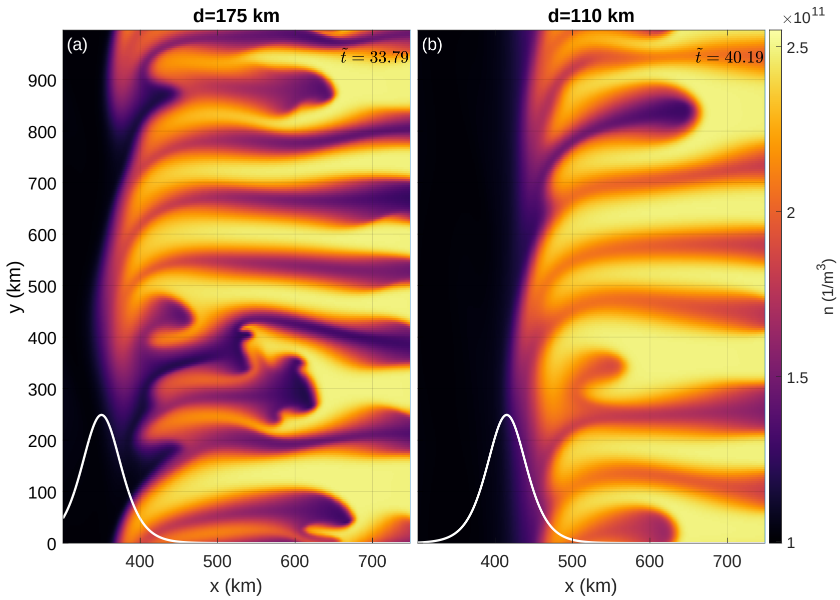

Figure 7. Plots of plasma density later in time for Figures 6(a) and (b). The velocity shear acts as a wall and prevents the GDI from propagating further in the equatorward direction.

The question arises as to what happens if the GDI from Figures 6(a) and 6(b) are allowed to continue growing until the GDI reaches the velocity shear. Figure 7 shows the plasma density from Figures 6(a) and (b) at a later time. The solid white curve represents the location of the velocity profile. What can be seen in both panels is that the velocity shear acts as a wall and prevents the GDI from propagating further equatorward. These results suggest that the GDI is not able to traverse the velocity channel. Therefore, if the GDI grows at the poleward density gradient and outside of the SAPS, it is not expected to also propagate into the SAPS.

The simulation from Figure 6(b) is rerun with a smaller y domain with more grid points such that the smallest resolvable wavelength in the y direction becomes 195.3 m, which is closer to GPS and SuperDARN radar resolvable scales. Figure 8 shows the turbulence cascade in the power spectra in x and y of the perturbed density divided by the total density and the perturbed electric potential. The power spectra are calculated by taking the Fourier transform in the x (y) direction and integrating over the instability region in the y (x) direction. Each spectrum has different power law fits that apply to different regions. The results are anisotropic with the x spectra showing smaller slopes than the y spectra for both quantities. The y spectra have a region between 1 and 10 km^{-1} that appears to follow power laws of -5/3 and -2 which have been observed by DMSP satellite data (Mishin & Blaunstein, 2008). These slopes also agree in the y direction with nonlinear GDI theory (M. J. Keskinen, 1984). The disagreements in the x direction with the nonlinear GDI theory could be due to the addition of the velocity shear and inertial effects.

Observations suggest that density irregularities are ubiquitous in the density trough and SAPS (Mishin et al., 2003; Mishin & Blaunstein, 2008). Figures 6 and 7 suggest that the GDI would not grow inside SAPS. The latitudinal width and gradient scale length of the velocity profile can be modified to determine if there are feasible conditions in which the GDI might evolve inside SAPS. Figure 9 shows the results when using Eq. 14 for V_y with $V_0^t = -1000$ m/s, $L_V^t = 10$ km, and w varying from 125 to 305 km. The bot-

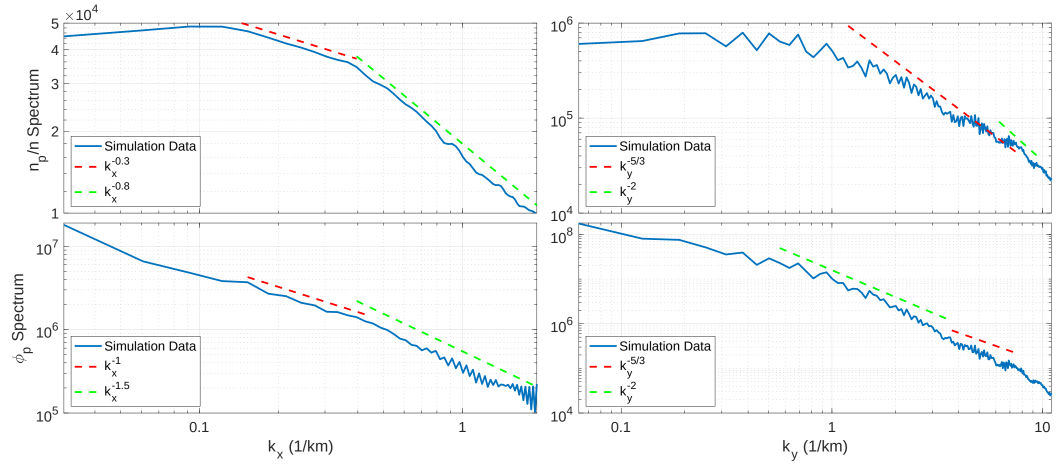

Figure 8. A plot of power spectra of the perturbed density divided by the total density and perturbed electric potential at $\tilde{t} = 6.45$ from a higher resolution simulation of Figure 6(b). The dashed red and green lines correspond to different power law fits for each spectrum. The power spectra are anisotropic with the x direction having smaller slopes than the y direction. The density and electric potential show differences between their power spectra in the x direction. In the y direction, the powers of -5/3 and -2 more closely match observed spectra in the region from 1 to 10 km^{-1} (Mishin & Blaunstein, 2008).

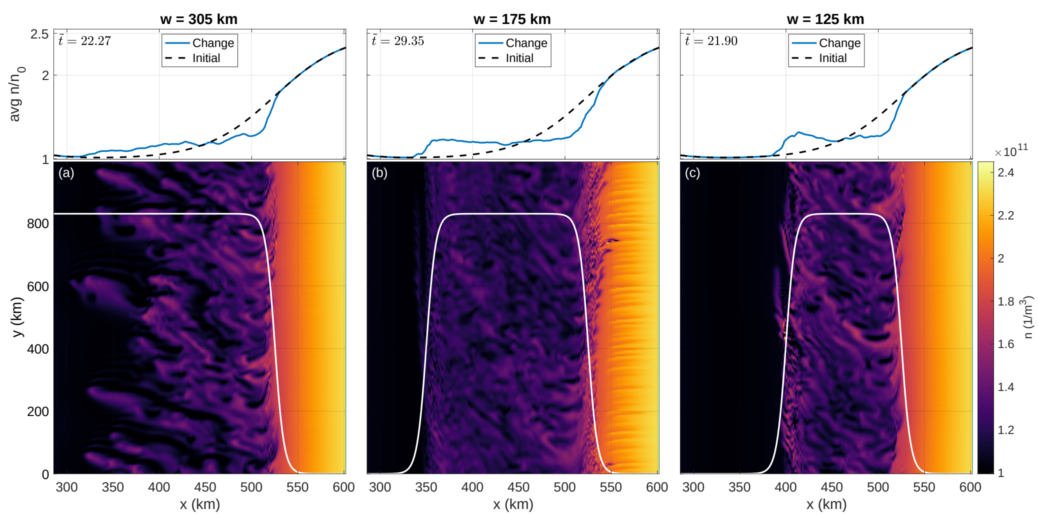

Figure 9. The bottom panels show plots of plasma density using Eq. 14 for the V_y initial conditions with $V_0^t = -1000$ m/s, $L_V^t = 10$ km, and w varying from 125 to 305 km. The top panels show the y averaged density normalized by n_0. The white curve represents the velocity profile. The velocity-impacted GDI propagates from the poleward density gradient in the equatorward direction. The equatorward velocity gradient stops the further propagation of the velocity-impacted GDI as can be seen in Panels (b) and (c). The result is a highly structured SAPS region. The turbulent mixing results in the average density appearing to have an effect that creates another region of approximately constant density.

tom panels show the plasma density with the white curve representing the velocity profile. The top panels show the average of the density over the y direction normalized by n_0. In all of the cases, the GDI seems to be heavily impacted by the larger velocity shear and propagates equatorward into the SAPS. The equatorward velocity gradient acts as a wall and appears to prevent further propagation equatorward as seen in Figures 9(b) and 9(c). The same type of growth also occurs for some larger L_V^t values, but at a slower rate. Additional features can be observed in Figure 9(b) poleward of the density gradient. Thin fingers are seen growing poleward, which could be due to a more traditional GDI developing in a new location further poleward from the stabilizing region of large velocity shear as observed in Figure 6. The top panels of Figure 9 show how the y averaged density, normalized by n_0, varies spatially, creating a region of approximately constant density within the velocity shear layer after turbulent mixing has occurred.

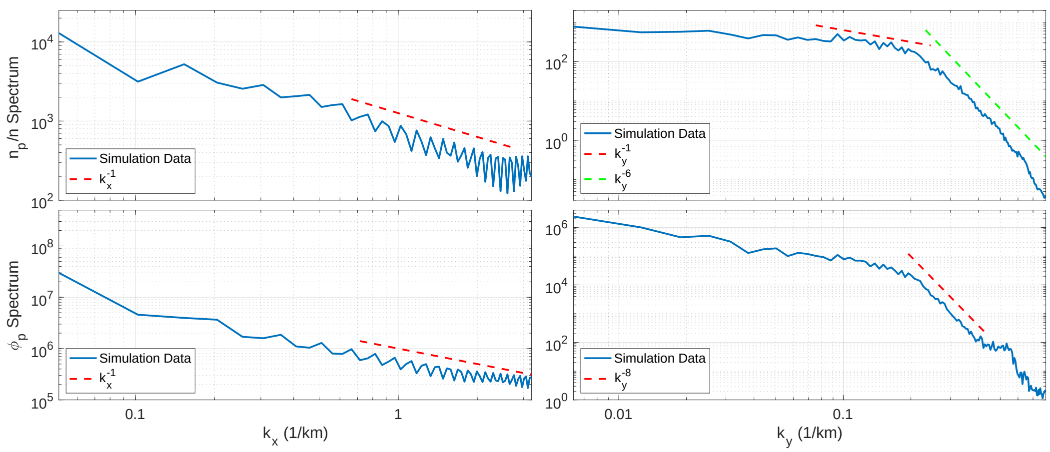

Figure 10. A plot of power spectra of the perturbed density divided by the total density and the perturbed electric potential at $\tilde{t} = 29.35$ of Figure 9(b) in the region from $x = 375$ km to $x = 500$ km. The dashed red and green lines represent different power law fits for each spectrum. The power spectra are anisotropic with the x direction having smaller slopes than the y direction. The x direction spectra are fairly close to those from Figure 8. However, the y direction spectra decay at a faster rate than those from Figure 8, suggesting that the velocity shear is impacting the GDI turbulence cascade.

The instability development in Figure 9 looks different from that of Figure 6. Figure 10 shows the power spectra of the late stage development of the instability from Figure 9(b). The x direction shows similar powers as Figure 8. The y direction, however, is vastly different, showing a steeper decay than Figure 8 with power laws of -6 for the density and -8 for the electric potential. This suggests that the velocity shear plays a substantial role in altering the irregularity development from a pure GDI case.

Despite this difference, certain trends of GDI growth still remain. The case in Figure 9(a) is considered with a smaller neutral wind ($u_x = -100$ m/s). Figure 11 shows how the growth rate changes from the previous $u_x = -500$ m/s case. The growth rate no longer follows the parabola that is described by Eq. 15 and shown in Figure 5, suggesting that the velocity shear has a large impact on the growth rate. However, the higher neutral wind produces a generally larger growth rate, which is consistent with GDI theory. This suggests that larger neutral wind speed will cause faster growth.

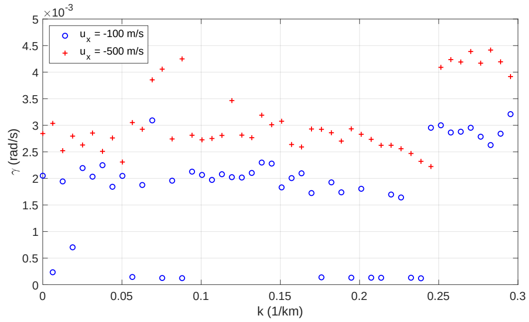

Figure 11. A plot of the growth rate versus wavenumber for simulations with different neutral winds. The red pluses represent the growth rate for the simulation shown in Figure 9(a). The blue circles represent the same case but with $u_x = -100$ m/s. Despite the growth looking substantially different from the expected growth described by Eq. 15 and Figure 5(b), the general trend of increasing the neutral wind does increase the instability growth rate. The red pluses are generally higher than the blue circles.

5 Summary and Conclusions

Density irregularities have been observed to occur in SAPS and their corresponding density troughs (Mishin et al., 2003; Foster et al., 2004; Oksavik et al., 2006; Mishin & Blaunstein, 2008). The GDI is hypothesized to be a potential cause of the density irregularities based on the geometry of the density gradient, the electric field, and the magnetic field. A 2D electrostatic fluid model is used to study the impact of velocity shear on GDI growth in SAPS. Simulation parameters are chosen based on the wide parameter spread of SAPS analyzed in Figure 3 based on 10 SAPS events.

For velocities modeled using a hyperbolic secant-squared profile to study the influence of the relative location of the velocity region and density gradients, the velocity shear acts as a damping mechanism for the GDI, which is established in the literature (Perkins & Doles III, 1975; J. Huba et al., 1983; J. D. Huba & Lee, 1983). This is explicitly shown in Figure 6 using an equatorward neutral wind. The velocity shear causes the GDI to grow further poleward of the maximum GDI growth location in Figure 6(b) and effectively damps the instability altogether in Figure 6(c). More generally, the results suggest that as d approaches 0, the GDI becomes more stabilized until eventually no growth is observed. The GDI also becomes more stabilized as the velocity increases. Thus for SAPS events in which the velocity shear significantly overlaps the density gradient, the GDI is not expected to be observed. However, if d is sufficiently large, then the GDI is expected to grow in the density gradient region but unable to cross into the SAPS due to the stabilizing effect of the velocity shear as shown in Figure 7. Thus, the model predicts that any GDI that grows outside of the SAPS region will remain outside of the SAPS region.

For this type of instability growth, the y direction turbulence spectra shown in Figure 8 of the poleward instabilities agree well with observations from DMSP satellites. Figure 3 from Mishin and Blaunstein (2008) shows the turbulence spectra following a power law with slopes of about -5/3 or -2 which is consistent with the results of the numerical model in this work between 1 and 10 km^{-1}. This further suggests that the GDI is a viable cause of turbulence outside of the velocity profile.

When the velocity is modeled using hyperbolic tangent profiles, decreasing the velocity gradient scale length induces a GDI at the poleward density gradient inside the SAPS region whose behavior is heavily impacted by the velocity shear as seen in Figure 9. This instability propagates equatorward until it reaches the equatorward velocity gradient. The power spectra of these density irregularities (Figure 10) differ substantially from the GDI that grows outside the SAPS region (Figure 8). This suggests that the velocity shear is changing the nature of the turbulence cascade. Observations in SAPS that show spectra of this nature might suggest that the density irregularities are generated by a shear-impacted GDI. Qualitatively, this instability resembles the collisional Kelvin-Helmholtz instability (KHI) (M. Keskinen et al., 1988). The general trend, however, of increasing the background neutral wind does increase the growth rate of this instability, which is consistent with the nature of the GDI. Zhang et al. (2015) have measured poleward neutral winds during SAPS and data from Mishin and Blaunstein (2008) suggest the existence of both poleward and equatorward neutral winds in different SAPS events. A poleward neutral wind will cause the density irregularities at the equatorward density gradient.

There exist situations in which the GDI is a viable candidate for turbulence generation in SAPS. The results indicate that the density irregularities that are generated cannot propagate through a region of velocity shear. This implies that if observations show irregularities on both sides of the SAPS velocity shear, there are likely multiple sources of the density irregularities. A more detailed fundamental physics study of the GDI and the potential role of the KHI constitutes future work.

Acknowledgments

This work was funded by NASA under grant number NASAMAG16_2-0050 and the Bradley Department of Electrical Engineering at Virginia Tech.

B. Kunduri thanks and acknowledges the support of NSF under grants AGS-1822056 and AGS-1839509.

The authors acknowledge access to the SuperDARN database via the Virginia Tech SuperDARN group and their website (`http://vt.superdarn.org/`). SuperDARN is a collection of radars funded by national scientific funding agencies of Australia, Canada, China, France, Italy, Japan, Norway, South Africa, the United Kingdom and the United States of America. GPS TEC data are obtained from the Madrigal database.

References

Buonsanto, M. J. (1999). Ionospheric storms—a review. *Space Science Reviews*, *88*(3-4), 563–601.

Canuto, C., Hussaini, M. Y., Quarteroni, A., Thomas Jr, A., et al. (2012). *Spectral methods in fluid dynamics*. Springer Science & Business Media.

Chisham, G., Lester, M., Milan, S., Freeman, M., Bristow, W., Grocott, A., ... others (2007). A decade of the super dual auroral radar network (superdarn): Scientific achievements, new techniques and future directions. *Surveys in geophysics*, *28*(1), 33–109.

Erickson, P., Beroz, F., & Miskin, M. (2011). Statistical characterization of the american sector subauroral polarization stream using incoherent scatter radar. *Journal of Geophysical Research: Space Physics*, *116*(A5).

Foster, J., & Burke, W. (2002). Saps: A new categorization for sub-auroral electric fields. *Eos, Transactions American Geophysical Union*, *83*(36), 393–394.

Foster, J., Erickson, P., Lind, F., & Rideout, W. (2004). Millstone hill coherent-scatter radar observations of electric field variability in the sub-auroral polarization stream. *Geophysical research letters*, *31*(21).

Foster, J., & Vo, H. (2002). Average characteristics and activity dependence of the subauroral polarization stream. *Journal of Geophysical Research: Space Physics*, *107*(A12), SIA–16.

Gondarenko, N., & Guzdar, P. (1999). Gradient drift instability in high latitude plasma patches: Ion inertial effects. *Geophysical research letters*, *26*(22), 3345–3348.

Guzdar, P., Gondarenko, N., Chaturvedi, P., & Basu, S. (1998). Three-dimensional nonlinear simulations of the gradient drift instability in the high-latitude ionosphere. *Radio Science*, *33*(6), 1901–1913.

Hoh, F. (1963). Instability of penning-type discharges. *The Physics of Fluids*, *6*(8), 1184–1191.

Huba, J., Ossakow, S., Satyanarayana, P., & Guzdar, P. (1983). Linear theory of the e× b instability with an inhomogeneous electric field. *Journal of Geophysical Research: Space Physics*, *88*(A1), 425–434.

Huba, J. D., & Lee, L. (1983). Short wavelength stabilization of the gradient drift instability due to velocity shear. *Geophysical research letters*, *10*(4), 357–360.

Keskinen, M., Basu, S., & Basu, S. (2004). Midlatitude sub-auroral ionospheric small scale structure during a magnetic storm. *Geophysical research letters*, *31*(9).

Keskinen, M., Mitchell, H., Fedder, J., Satyanarayana, P., Zalesak, S., & Huba, J. (1988). Nonlinear evolution of the kelvin-helmholtz instability in the high-latitude ionosphere. *Journal of Geophysical Research: Space Physics*, *93*(A1), 137–152.

Keskinen, M. J. (1984). Nonlinear theory of the e× b instability with an inhomogeneous electric field. *Journal of Geophysical Research: Space Physics*, *89*(A6), 3913–3920.

Kunduri, B., Baker, J., Ruohoniemi, J., Thomas, E., Shepherd, S., & Sterne, K. (2017). Statistical characterization of the large-scale structure of the subauroral polarization stream. *Journal of Geophysical Research: Space Physics*, *122*(6), 6035–6048.

Lin, D., Wang, W., Scales, W. A., Pham, K., Liu, J., Zhang, B., … Maimaiti, M. (2019). Saps in the 17 march 2013 storm event: Initial results from the coupled magnetosphere-ionosphere-thermosphere model. *Journal of Geophysical Research: Space Physics*, *124*(7), 6212–6225.

Makarevich, R. A. (2014). Symmetry considerations in the two-fluid theory of the gradient drift instability in the lower ionosphere. *Journal of Geophysical Research: Space Physics*, *119*(9), 7902–7913.

Makarevich, R. A. (2019). Toward an integrated view of ionospheric plasma instabilities: 3. explicit growth rate and oscillation frequency for arbitrary altitude. *Journal of Geophysical Research: Space Physics*, *124*(7), 6138–6155.

Mishin, E., & Blaunstein, N. (2008). Irregularities within subauroral polarization stream-related troughs and gps radio interference at midlatitudes. *Midlatitude Ionospheric Dynamics and Disturbances, Geophys. Monogr. Ser*, *181*, 291–295.

Mishin, E., Burke, W., Huang, C., & Rich, F. (2003). Electromagnetic wave structures within subauroral polarization streams. *Journal of Geophysical Research: Space Physics*, *108*(A8).

Mitchell Jr, H., Fedder, J., Keskinen, M., & Zalesak, S. (1985). A simulation of high latitude f-layer instabilities in the presence of magnetosphere-ionosphere coupling. *Geophysical research letters*, *12*(5), 283–286.

Oksavik, K., Greenwald, R., Ruohoniemi, J., Hairston, M., Paxton, L., Baker, J., … Barnes, R. (2006). First observations of the temporal/spatial variation of the sub-auroral polarization stream from the superdarn wallops hf radar. *Geophysical research letters*, *33*(12).

Ossakow, S., Chaturvedi, P., & Workman, J. (1978). High-altitude limit of the gradient drift instability. *Journal of Geophysical Research: Space Physics*, *83*(A6), 2691–2693.

Perkins, F., & Doles III, J. (1975). Velocity shear and the e × b instability. *Journal of Geophysical Research*, *80*(1), 211–214.

Rideout, W., & Coster, A. (2006). Automated gps processing for global total electron content data. *GPS solutions*, *10*(3), 219–228.

Ruohoniemi, J., Greenwald, R., Baker, K., Villain, J., & McCready, M. (1987). Drift motions of small-scale irregularities in the high-latitude f region: An experimental comparison with plasma drift motions. *Journal of Geophysical Research: Space Physics*, *92*(A5), 4553–4564.

Schunk, R. W., Banks, P. M., & Raitt, W. J. (1976). Effects of electric fields and other processes upon the nighttime high-latitude f layer. *Journal of Geophysical Research*, *81*(19), 3271–3282.

Simon, A. (1963). Instability of a partially ionized plasma in crossed electric and magnetic fields. *The physics of fluids*, *6*(3), 382–388.

Spiro, R., Heelis, R., & Hanson, W. (1978). Ion convection and the formation of the mid-latitude f region ionization trough. *Journal of Geophysical Research: Space Physics*, *83*(A9), 4255–4264.

Thomas, E., Baker, J. B., Ruohoniemi, J. M., Clausen, L. B., Coster, A., Foster, J., & Erickson, P. (2013). Direct observations of the role of convection electric field in the formation of a polar tongue of ionization from storm enhanced density. *Journal of Geophysical Research: Space Physics*, *118*(3), 1180–1189.

Wang, H., Ridley, A. J., Lühr, H., Liemohn, M. W., & Ma, S. Y. (2008). Statistical study of the subauroral polarization stream: Its dependence on the cross–polar cap potential and subauroral conductance. *Journal of Geophysical Research: Space Physics*, *113*(A12).

Yu, Y., Jordanova, V., Zou, S., Heelis, R., Ruohoniemi, M., & Wygant, J. (2015). Modeling subauroral polarization streams during the 17 march 2013 storm. *Journal of Geophysical Research: Space Physics*, *120*(3), 1738–1750.

Zhang, S.-R., Erickson, P. J., Foster, J. C., Holt, J. M., Coster, A. J., Makela, J. J., ... others (2015). Thermospheric poleward wind surge at midlatitudes during great storm intervals. *Geophysical Research Letters*, *42*(13), 5132–5140.

Zheng, Y., Brandt, P. C., Lui, A. T., & Fok, M.-C. (2008). On ionospheric trough conductance and subauroral polarization streams: Simulation results. *Journal of Geophysical Research: Space Physics*, *113*(A4).